A System for MRI-guided Prostate Interventions[†]

S.P. DiMaio[1], G.S. Fischer[2], S.J. Haker[1], N. Hata[1], I. Iordachita[2], C.M. Tempany[1], R. Kikinis[1], G. Fichtinger[2]

[1]*Surgical Planning Lab, Department of Radiology*
Brigham and Women's Hospital, Harvard University
Boston, MA, simond@bwh.harvard.edu

[2]*Center for Computer Integrated Surgery*
Johns Hopkins University
Baltimore, MD, gabor@cs.jhu.edu

Abstract—Numerous studies have demonstrated the efficacy of image-guided needle-based therapy and biopsy in the management of prostate cancer. Magnetic Resonance Imaging (MRI) is an ideal modality for guiding and monitoring such interventions due to its excellent visualization of the prostate, its sub-structure and surrounding tissues. However, the accuracy of needle placement is limited by image fidelity, needle template guides, needle deflection and tissue deformation. We present a preliminary study of the key sources of needle placement error in actual clinical cases. To address these errors, we have designed a comprehensive robotic assistant system with the following features: high-fidelity MRI imaging, advanced planning and targeting with statistical anatomical atlases and multi-parametric imaging, improved navigation based on direct image feedback, and steady needle placement with a robotic manipulator. The prostate biopsy and brachytherapy procedures are to be performed entirely inside a 3T closed-bore MRI scanner. We present a detailed design of the robotic manipulator and associated planning and targeting systems.

Index Terms—MRI-guided interventions, needle placement, surgical planning, medical robotics, prostate cancer

I. INTRODUCTION

One out of every six men in the United States will be diagnosed with prostate cancer at some point in his life [1]. The definitive method of diagnosis is core needle biopsy, and each year approximately 1.5M core needle biopsies are performed, yielding about 220,000 new prostate cancer cases [1]. If the cancer is found to be confined to the prostate, then low-dose-rate permanent brachytherapy—performed by implanting a large number (50-150) of radioactive pellets/seeds into the prostate using thin needles (typically 18G)—is a common treatment option [2]. A complex seed distribution pattern must be achieved with great accuracy in order to eradicate the cancer while minimizing radiation toxicity to adjacent healthy tissues. There are over 40,000 brachytherapies performed in the U.S. each year and the number is steadily growing [3]. Transrectal Ultrasound (TRUS) is the current "gold standard" for guiding both biopsy and brachytherapy due to its fast image acquisition rate, low cost, and apparent ease of use [4]. However, current TRUS-guided biopsy has a detection rate of 20-30% [5]. Furthermore, TRUS-guided brachytherapy cannot effectively monitor the implant procedure as implanted seeds cannot easily be seen in the images. MRI seems to possess many of the capabilities that TRUS is lacking. It has high sensitivity for detecting prostate tumors, high spatial resolution, excellent soft tissue contrast, and multiplanar

volumetric imaging capabilities [6]. Further, MR image registration techniques [7] allow images obtained before the day of the procedure to be used for intra-procedural targeting and planning. Therefore, MR imaging techniques that are sensitive to cancer but too time consuming for intraoperative use, such as diffusion imaging [8] and spectroscopic studies [9], as well as derived images designed to enhance specificity [10] or to incorporate knowledge of the most likely locations of tumors within the gland [11], can be fully utilized. Closed high-field MRI, however, has not been widely adopted for prostate interventions because high magnetic fields and confined physical space present formidable challenges for performing needle placement procedures in-bore.

The clinical efficacy of MRI-guided prostate brachytherapy and biopsy was demonstrated by D'Amico, Tempany, et al. at the Brigham and Women's Hospital using a 0.5T open-MRI scanner to plan and monitor transperineal needle placement [12], [13]. The needles were inserted manually using a plastic guide comprising a grid of holes, with the patient oriented in the lithotomy position, similarly to the TRUS-guided approach. Zangos et al. used a transgluteal approach with 0.2T MRI, but did not specifically target the tumor foci [14]. Susil et al. described four cases of transperineal prostate biopsy in a closed-bore scanner, where the patient was moved out of the bore for needle insertions and then placed back into the bore to confirm satisfactory placement [15]. Beyersdorff et al. performed targeted transrectal biopsy in a 1.5T MRI unit with a passive articulated needle-guide and have reported 12 cases of biopsy to date [16].

Robotic assistance has been investigated for guiding instrument placement in MRI, beginning with neurosurgery [17] and later percutaneous interventions [18], [19]. Chinzei et al. developed a general-purpose robotic assistant for open MRI [20] that was subsequently adapted for transperineal intra-prostatic needle placement [21]. Krieger et al. presented a 2-DOF passive, un-encoded and manually manipulated mechanical linkage to aim a needle guide for transrectal prostate biopsy with MRI guidance [22]. With three active tracking coils, the device is visually servoed into position and then the patient is moved out of the scanner for needle insertion. Other recent developments in MRI-compatible mechanisms include haptic interfaces for fMRI [23] and multi-modality actuators and robotics [24].

This work presents quantitative analysis of errors occurring in conventional prostatic needle placement and introduces the design of a comprehensive robot-assisted

system for transperineal prostate needle placement in 3T closed-bore MRI. The system integrates an image-based target planning interface, a robotic placement mechanism for remote manipulation of the needle in the magnet bore without moving the patient out of the imaging space, as well as robot and needle tracking for navigation and control. This enables the use of real-time multi-modality imaging for precise placement of needles in soft tissues. In addition to structural images, protocols for diffusion imaging and MR spectroscopy will be available intraoperatively, promising enhanced visualization and targeting of pathologies. Accurate and robust needle placement devices, navigated based on such image guidance are becoming invaluable clinical tools and have clear applications in several other organ systems.

The paper is organized as follows: Section II presents a quantitative analysis of conventional MRI-guided intraprostatic needle placement. Section III describes the architecture of the proposed computer-assisted clinical needle placement system. Section IV presents the planning and targeting module. Section V describes the design of the MRI-compatible manipulator, followed by a brief conclusion.

II. QUANTIFICATION OF NEEDLE MISPLACEMENT

Although MRI-guided biopsies that target suspected tumor foci appear to yield higher detection rates than statistical sampling [25], the accuracy of needle placement in transperineal prostate interventions has never been formally and quantitatively evaluated. Determining the accuracy of needle placement within the targeted tissue is difficult using current forms of navigation and guidance techniques. Purely MRI-based evaluation can introduce errors that are much larger than the maximum needle placement error tolerated in the biopsy or brachytherapy procedures, mainly due to imaging artifacts.

We have conducted a number of preliminary studies in order to investigate the accuracy of needle placement during MRI-guided transperineal prostate biopsy at BWH. From this, a taxonomy of factors that contribute to lower-than-desired accuracy is being developed. In an analysis of clinical cases we measured the distances between the pre-planned targeted locations and the actual needle tip visible in Fast Gradient Recalled (FGR) MR images taken intraoperatively. In a statistical analysis with $n = 4$ patients, the mean distance between the pre-planned locations and the actual measured needle tip coordinates for all biopsy locations was 6.93mm, with a standard deviation of 0.93mm. Susil et al. have also measured transperineal biopsy needle placement accuracy using 1.5T MRI guidance and significantly stiffer 14G needles. Mean needle-placement accuracy was 2.1mm, with a maximum needle-placement error of 4.4mm [15].

Phantom experiments were used to classify sources of error that contribute to this inaccuracy. Placement error due to needle deflection was measured using a rectangular box with seven holes on one side aligned directly with seven target points on the other side of the box. This allowed us to simulate actual needle insertions through a template, and to quantify the needle deflection. Two 18G needles were used—one with an asymmetrically bevelled tip and another with a symmetrical trihedral bevel. Each was inserted into three different phantom types: gelatine, bovine liver sample, and bovine muscle tissue. Two readers measured the resulting deflection of the needle tip at the distal end of the box. The mean tip error was measured to be 0.87mm, 2.47mm, and 8.87mm in gelatine, Bovine Liver, and Bovine Muscle samples respectively. In a second experiment we quantified the shift of the needle artifact in the images. A biopsy needle was clamped into the phantom enclosure and immersed in a gadolinium-doped water solution (1:500 Gd-DTPA/water ratio, gadopentetate dimeglumine, Berlex Magnevist). Four sets of MR images were taken with the frequency encode direction in the R/L and A/P directions and slice thicknesses of 5mm and 7mm. The difference between the actual position of the needle (determined from fiducials affixed to the phantom) and the center of the artifact were measured. We found that changing the slice thickness and frequency encoding direction does affect visualization of true needle position, and may therefore impact needle placement when repeated insertions are made to compensate for observed misplacement.

These preliminary experiments indicate that placement errors are significant with respect to lesion size and proximity to crital structures, particularly due to needle deflection (corroborated by Susil's results using stiffer 14G needles). With better control of needle and tissue deflection, as well as with tracking of actual needle position, it may be possible to reduce needle placement errors that we observe in clinical practice. In the following sections, we describe a comprehensive robotic assistant system that aspires to achieve this goal.

III. SYSTEM LAYOUT AND ARCHITECTURE

A comprehensive computer-integrated needle placement system has been designed in order to accurately target planned tissue sites by minimizing the misplacement effects described above. The complete system comprises two major modules that are integrated with a standard commercial high-field diagnostic MRI scanner, namely: 1) a visualization, planning and navigation engine and 2) a needle placement robot. The architecture of this system is outlined in Figure 1. Blocks **a** and **b** represent target planning by visual inspection of multi-parametric fused image datasets and by applying statistical atlases, as described in Section IV. We use the 3D Slicer software interface for this purpose (www.slicer.org). The kinematics of the needle trajectories required to reach these desired targets is evaluated here, subject to anatomical constraints, as well as constraints of the needle placement mechanism. Device and needle navigation are shown in blocks **c**, **d** and **e**, which are enclosed in a loop that represents device/needle positioning and sensing/localization that iterate until the needle trajectory leads to placement at the desired target. Device and needle tracking may be image-based, as illustrated by block **c** and it's connection with block **h**. Blocks **d** and **e**
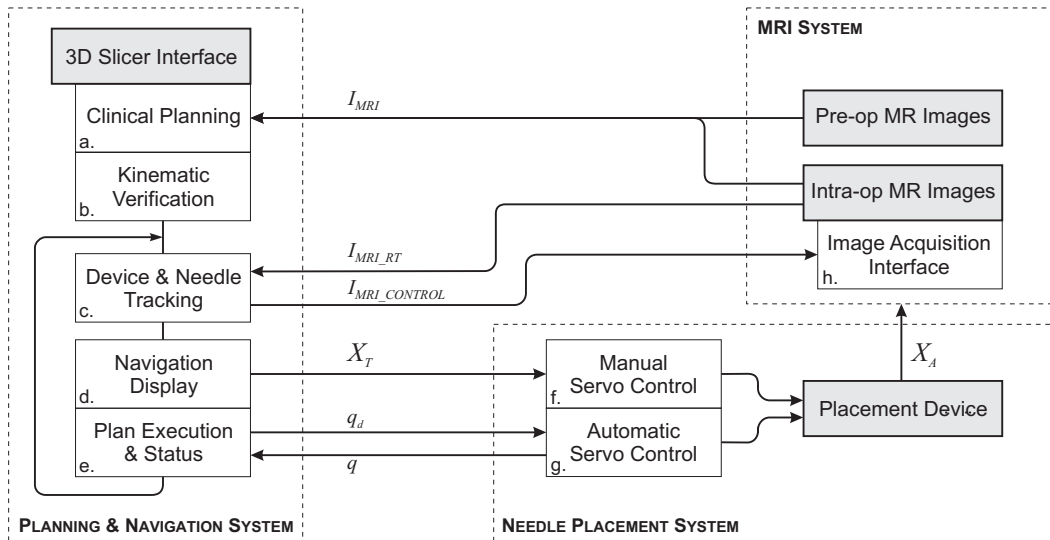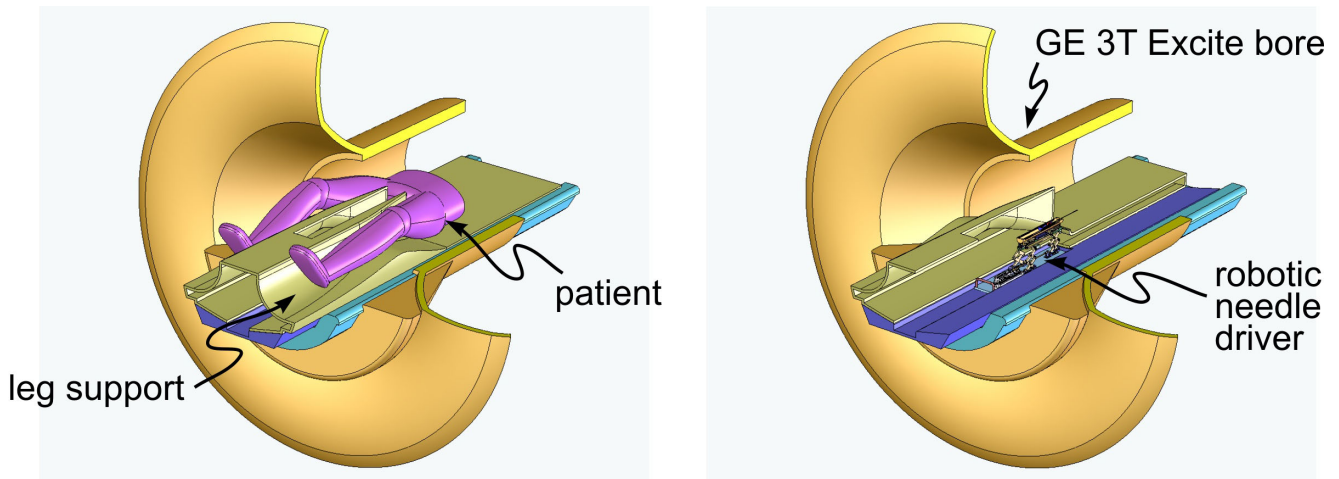
Fig. 1.   System Architecture.

Fig. 2.   Patient layout and system configuration.

guide manual or automatic control of the needle positioning device, based on this closed image-based servo loop that provides the ability to compensate for the needle and tissue deflection effects described in Section IV. Physical positioning and insertion of the needle occur in **f** and **g**, by a mechanical mechanism that provides remote operation of the needle while the patient is positioned within the magnet bore. This mechanism may either be manually operated or motorized, via a pneumatic coupling. The position of the patient and the mechanism in the bore is shown in Figure 2. The patient's legs are placed on a leg support that provides a "tunnel" of access to the perineum. A compact robotic needle driver mechanism is placed into this tunnel, as shown, and is described in detail in Section V.

IV. PLANNING AND NEEDLE TARGETING

Prostate MRI, especially with combined endorectal and phased array coils, provides images of high resolution and is used in prostate cancer staging as well as in the determination of extraprostatic disease. The T1- and T2-weighted images help to differentiate between post-biopsy hemorrhage and prostate cancer, which presents as a low T1 and low T2 lesion, while hemorrhage presents as a high T1 and low T2 lesion. Recent advances in MR prostate imaging hold promise for increased specificity and sensitivity. For example, contrast enhanced images are proving to be important for distinguishing between normal and cancerous tissues. Indeed, perfusion of bladder and prostate cancers may be increased relative to normal tissue, and is detected as signal enhancement following intravenous injection of MR contrast agents such as Gadolinium-DTPA [26], [27]. In recent years, in vivo MR proton spectroscopy has become an important technique for characterizing prostate tissue by evaluating its metabolic activity. Several groups have shown the utility of 1H spectroscopy to detect biochemical markers in the prostate that can be used to differentiate prostate cancer from normal tissue, or from benign prostatic hyperplasia (BPH) in vivo [9]. Finally, recent studies, including [8], have demonstrated decreased diffusion coefficients in malignant versus non-cancerous peripheral zone.

Metabolic information from spectroscopy, diffusion weighted and dynamic contrast pre-treatment MR data

can be combined with routine T2 and T1 weighted MR images to allow precise tumor targeting. The information from pre-procedure and intra-procedure images are registered, and target lesions are identified by a radiologist. A major difficulty in registration comes from the shape changes that can occur in soft tissues between imaging sessions. This shape change may, for example, be the result of changes in patient position necessitated by the procedures. Our non-rigid registration method models basic biomechanical properties of soft tissue [7]. In summary, the method involves the following steps: 1) A 3D tetrahedral model of the entire prostate is created from segmented pre-operative 1.5T images; 2) the boundary surface of the capsule is extracted from this tetrahedral mesh and is registered to a corresponding capsule surface obtained from intra-operative images; 3) the surface point matches from step 2 are used as boundary conditions when solving a finite element-based system of equations which models the volumetric deformation field within the gland; and, 4) the volumetric deformation field from step 3 is used to interpolate pre-operative imaging data.

Once targets are identified and the biopsy procedure begins, we can provide the physician with feedback on the position of the needle relative to the targets. Real-time (every three seconds) 2D FGR images of the prostate obtained throughout the biopsy procedure allow visualization of the prostate gland, rectum, bladder, catheter and needle position. However, these FGR images do not provide adequate contrast for visualization of sub-structures of the gland, namely the peripheral zone (PZ) and suspicious targets. These sub-structures are critical for precise biopsy sampling, and are provided by T2W imaging obtained before the procedure begins. Our method for combining FGR and T2W imaging for feedback to the physician will be similar to what is currently done within our 0.5T open-bore system [25], using the 3D Slicer (www.slicer.org) visualization system. The Slicer effectively enables direct T2W visualization of the peripheral zone of the prostate with real-time FGR imaging visualized in the same frame of reference. As each 2D real-time FGR image is obtained, either an axial or coronal T2W image data set is resampled (both are imaged at the beginning of the procedure), pixel-by-pixel, at the same spatial locations as those of the FGR image. To limit interpolation artifacts, the particular choice of T2W data set sampled depends on whether the FGR image is closer in orientation to axial or coronal. Alternating views of the most recent real-time FGR and resampled T2W images are presented on a monitor in the bore of the scanner. A 1-2 second delay between the alternating images is used. In this way, the radiologist may see the needle artifact and its position relative to the PZ and suspicious foci. Using the described method to combine FGR and T2W images, we have successfully guided the biopsy needle to targets and assured proper placement of the needle within the peripheral zone during 0.5T cases (see Figure 3).
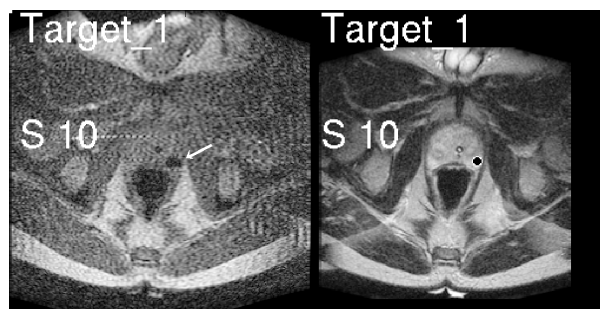

Fig. 3. Images displayed for the physician during the procedure. FSE real-time image (L) showing needle artifact (arrow) and T2 weighted (R) pre-procedure image with peripheral zone target marked. Distance to target (Superior 10mm) is also displayed.

V. NEEDLE PLACEMENT ROBOT

The design of the robotic manipulator accommodates the confined workspace at the patient's perineum, while maintaining a compact profile to prevent interference with the patient, the scanner and adjacent equipment. The kinematic requirements are: 100mm of horizontal and vertical translation, $\pm 15°$ of rotation in the horizontal plane, $15°$ of elevation in the vertical plane, and 120mm needle insertion including independent cannula retraction for brachytherapy. Planar motion bar mechanisms made of non-metallic materials are used, while the mechanism design employs kinematics with decoupled motion axes that simplifies control, allows appropriate actuator alignment and increased system rigidity.

The four primary degrees of freedom (DOF) of the base are broken into two decoupled 2-DOF planar motions. Motion in the sagittal plane includes 100mm of vertical travel, and up to $15°$ of positive elevation angle. This is achieved using a modified scissor lift mechanism that is traditionally used for plane parallel motion. By coupling two such mechanisms, as shown in Figure 4(a), the two desired DOF can be achieved. Stability is increased by using a pair of such mechanisms in the rear. For prismatic motion alone, both slides are moved together. To tilt the needle, the front slide remains fixed and the rear is moved relative to it. For decoupled motion the actuator for the rear slide is fixed to the carriage of the primary motion linear drive. Motion in the coronal plane is accomplished using a second planar bar mechanism. Both prismatic and rotational motions can be realized by coupling two straight-line motion mechanisms, as shown in Figure 4(b). This mechanism design allows for bilateral motion about the center of the robot, actuated by a modified compact pneumatic cylinder oriented along the bore axis (B_0), thus minimizing the overall width of the device. Figure 4(b) shows the horizontal motion stage in the 1-DOF configuration where only translation is available. This is accomplished by linking the front and rear mechanisms with a connecting bar (L_c). Horizontal rotational motion can be added by replacing the rigid connecting bar, L_c, with a pneumatic cylinder.

The complete assembly is shown in Figure 5. The robot assumes a home position on a manual slide that
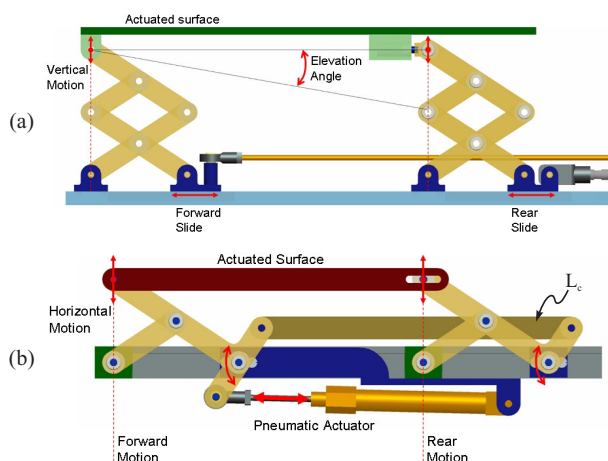
Fig. 4. (a) The mechanism for motion in the vertical plane allows vertical travel and actuation of elevation angle. (b) For plane parallel horizontal motion, both translation and rotation are provided.

moves into the tunnel between the patient's legs and docks in a known, repeatable position relative to the scanner. Numerous animated motion sequences were performed in a CAD environment seen earlier in Figure 2, to determine that the robot meets all kinematic requirements. The robot is designed to be constructed entirely of non-ferrous materials; conductive materials are used sparingly, and the links and connections are made of plastic (Polyetherimide, Ultem). As in [22], the manual gross positioning slide is permitted to contain non-ferrous metal parts, since they will be positioned sufficiently far from the isocenter.
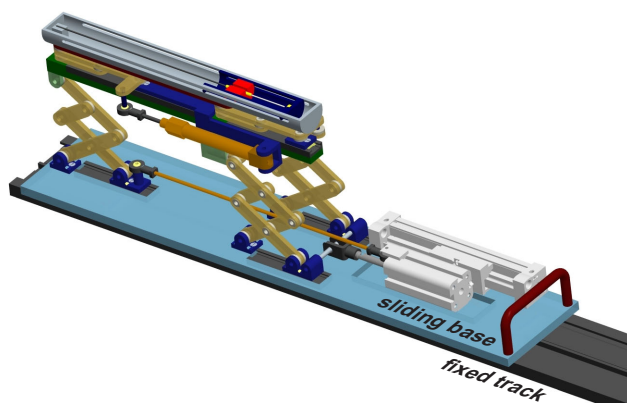

Fig. 5. Robot mechanism shown on manual gross positioning slide with brachytherapy end effector.

The MRI environment excludes most conventional electro-dynamic actuation devices. Transmission mechanisms can be used to mechanically couple the manipulator located in the MRI scanner to standard actuators situated outside the high field; examples of suitable transmissions include flexible drive shafts [22], push-pull cables and hydraulic/pneumatic couplings [23]. We have selected pneumatic actuators because they offer relatively high speed and power for their weight, and due to the large selection of components available and readily available compressed air supply. To maintain compatibility with the magnetic field,

we chose piezoelectrically actuated valves (as opposed to standard solenoid coils) to control the cylinders. The pneumatic cylinders will not interfere with the magnetic field provided that they do not include ferrous materials.

Linear optical encoders seem to have excellent potential for joint encoding in the MRI environment. We tested a US Digital EM1-0-500 encoder module with PC5 differential line driver in a 3T MRI scanner for functionality and in a 1.5T scanner for imaging compatibility. Test results in Figure 6 show that 50mm beyond the encoder, situated at the scanner isocenter on top of a cylindrical phantom, there is little or no induced artifact (GE Signa Excite 1.5T scanner). This is a most promising result, indicating the suitability of linear optical encoders for joint measurement, provided that they are placed sufficiently far from the magnet's isocenter.
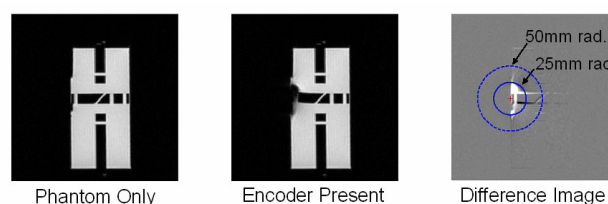

Fig. 6. MR compatibility trial of optical encoder in a 1.5T scanner.

Dynamic global registration between the robot and scanner is not necessary, as in the beginning of the intervention the needle placement robot assumes a precisely calibrated home position relative to the scanner's coordinate system. For high-level control and monitoring, the MR images can be used to directly locate the robot's end effector using embedded fiducials.

Proportional pressure valves are our first choice for pneumatic servo control of this robot (Hoerbiger-Origa PRE-U piezo valve). With pressure-based control, pressures on both sides of the piston are regulated continuously with respect to each other based on the cylinder's position error using two independent valves; this allows the actuator to be moved smoothly while maintaining high stiffness. The valves and their associated electrical and pneumatic distribution will be in a non-ferrous, RF-shielded enclosure situated at the foot of the bed. The use of piezo valves allows their placement inside the scanner room, which enables shorter pneumatic tubing runs resulting in a more stable system with a faster response.

Control software is implemented on a PC using the Real Time Application Interface (RTAI) Linux kernel extension. The Low Power Motor Control (LoPoMoCo) hardware interface, developed by [28], is used for low-level control of the robot; each ISA board supports 8 analog outputs, 8 analog inputs, 4 incremental encoder inputs and general purpose IO. To increase portability of the system, an ISA-to-USB converter (ARS Technologies Inc. USB2ISA Adapter) enables real-time robot control from an RTAI Linux-based laptop PC located in the MR console room.

Needle insertion will be performed under cooperative control; an encoded slider will be manipulated by the

clinician, while the robotic needle driver follows. The reason for keeping a human in the loop is to increase the safety of the needle insertion, and to allow the physician to use live MRI images to help monitor progress and positioning. Visual servoing of the robot and bevel-based steering of the needle [29], as well as fully automated insertion, will be investigated in future design iterations.

VI. CONCLUSION

MRI-guided percutaneous interventions are expected to make an important contribution to the management of prostate cancer. The ability of MRI to image many different physiological parameters within tissues is of interest in the planning and staging of clinical interventions; however, the accuracy of interventional guidance and navigation of instruments in soft tissues has fallen behind the fidelity and resolution of new planning and targeting methods, thus limiting the utility of these methods, as well as our ability to validate them. We have described a novel computer-assisted planning and placement system for percutaneous prostate intervention. We aspire to significantly reduce misplacement and placement uncertainty that is now on the order of $5 - 10$mm. This work is also of relevance to other organ systems and diseases that can benefit from targeted needle placement inside an MRI scanner.

REFERENCES

[1] A. Jemal, "Cancer statistics, 2004," in *CA Cancer J Clin*, vol. 54(8), 2004.
[2] J. C. Blasko, T. Mate, J. E. Sylvester, P. D. Grimm, and W. Cavanagh, "Brachytherapy for carcinoma of the prostate: techniques, patient selection, and clinical outcomes," in *Semin Radiat Oncol*, vol. 12(1), pp. 81–94, 2002.
[3] M. R. Cooperberg, D. P. Lubeck, M. V. M. S. S. Mehta, and P. R. Carroll, "The changing face of low-risk prostate cancer: trends in clinical presentation and primary management," in *J Clin Oncol*, vol. 22(11), pp. 2141–9, 2004.
[4] J. C. Presti Jr., "Prostate cancer: assessment of risk using digital rectal examination, tumor grade, prostate-specific antigen, and systematic biopsy," in *Radiol Clin North Am*, vol. 38(1), pp. 49–58, 2000.
[5] M. K. Terris, E. M. Wallen, and T. A. Stamey, "Comparison of mid-lobe versus lateral systematic sextant biopsies in detection of prostate cancer," in *Urol Int*, vol. 59, pp. 239–242, 1997.
[6] K. K. Yu and H. Hricak, "Imaging prostate cancer," in *Radiol Clin North Am*, vol. 38(1), pp. 59–85, 2000.
[7] S. Haker, S. Warfield, and C. Tempany, "Landmark-Guided Surface Matching and Volumetric Warping for Improved Prostate Biopsy Targeting and Guidance," in *Lecture Notes in Computer Science*, vol. 3216, pp. 853–861, Jan. 2004.
[8] S. Haker, A. Barnes, S. Maier, C. Tempany, and R. Mulkern, "Diffusion Tensor Imaging for Prostate Cancer Detection: Preliminary Results from a Biopsy-Based Assessment," in *International Society for Magnetic Resonance in Medicine, 13th Scientific Meeting and Exhibition, Proceedings*, 2005.
[9] J. Kurhanewicz, D. Vigneron, R. Males, M. Swanson, K. Yu, and H. Hricak, "The prostate: MR imaging and spectroscopy. Present and Future," in *Radiol Clin North Am*, vol. 38, pp. 115–138, 2000.
[10] I. Chan, W. Wells, R. Mulkern, S. Haker, J. Zhang, K. Zou, S. Maier, and C. Tempany, "Detection of prostate cancer by integration of line-scan diffusion, T2-mapping and T2-weighted MR imaging; a multichannel statistical classifier," in *Med Phys*, vol. 30, pp. 2390–2398, 2003.
[11] D. Shen, Z. Lao, J. Zeng, E. Herskovits, G. Fichtinger, and C. Davatzikos, "A Statistical Atlas of Prostate Cancer for Optimal Biopsy," in *Lect. Notes in Comp. Sci.*, vol. 2208, pp. 416–424, 2001.
[12] V. D'Amico, R. Cormack, C. M. Tempany, S. Kumar, G. Topulos, H. M. Kooy, and C. N. Coleman, "Real-time magnetic resonance image-guided interstitial brachytherapy in the treatment of select patients with clinically localized prostate cancer," in *International Journal of Radiation Oncology*, vol. 42, pp. 507–515, Oct. 1998.
[13] A. V. D'Amico, C. M. Tempany, R. Cormack, N. Hata, M. Jinzaki, K. Tuncali, M. Weinstein, and J. P. Richie, "Transperineal magnetic resonance image guided prostate biopsy," in *J Urol*, vol. 164(2), pp. 385–7, 2000.
[14] S. Zangos, K. Eichler, K. Engelmann, M. Ahmed, S. Dettmer, C. Herzog, W. Pegios, A. Wetter, T. Lehnert, M. G. Mack, and T. J. Vogl, "MR-guided transgluteal biopsies with an open low-field system in patients with clinically suspected prostate cancer: technique and preliminary results," in *Eur Radiol*, vol. 15(1), pp. 174–82, 2005.
[15] R. C. Susil, K. Camphausen, P. Choyke, E. R. McVeigh, G. S. Gustafson, H. Ning, R. W. Miller, E. Atalar, C. N. Coleman, and C. Ménard, "System for prostate brachytherapy and biopsy in a standard 1.5 T MRI scanner," in *Magnetic Resonance in Medicine*, vol. 52(3), pp. 683–687, 2004.
[16] D. Beyersdorff, A. Winkel, B. Hamm, S. Lenk, S. A. Loening, and M. Taupitz, "MR imaging-guided prostate biopsy with a closed MR unit at 1.5 T: initial results," in *Radiology*, vol. 234, pp. 576–581, 2005.
[17] K. Masamune, E. Kobayashi, Y. Masutani, M. Suzuki, T. Dohi, H. Iseki, and K. Takakura, "Development of an MRI-compatible needle insertion manipulator for stereotactic neurosurgery," in *J Image Guid Surg*, vol. 1(4), pp. 242–8, 1995.
[18] A. Felden, J. Vagner, A. Hinz, H. Fischer, S. O. Pfleiderer, J. R. Reichenbach, and W. A. Kaiser, "ROBITOM-robot for biopsy and therapy of the mamma," in *Biomed Tech (Berl)*, vol. 47 Suppl 1 Pt 1, pp. 2–5, 2002.
[19] E. Hempel, H. Fischer, L. Gumb, T. Hohn, H. Krause, U. Voges, H. Breitwieser, B. Gutmann, J. Durke, M. Bock, and A. Melzer, "An MRI-compatible surgical robot for precise radiological interventions," in *Computer Aided Surgery*, pp. 180–191, Apr. 2003.
[20] K. Chinzei, N. Hata, F. A. Jolesz, and R. Kikinis, "MR compatible surgical assist robot: system integration and preliminary feasibility study," in *Medical Image Computing and Computer Assisted Intervention*, vol. 1935, pp. 921–933, Oct. 2000.
[21] S. P. DiMaio, S. Pieper, K. Chinzei, G. Fichtinger, C. Tempany, and R. Kikinis, "Robot assisted percutaneous intervention in open-MRI," in 5th *Interventional MRI Symposium*, p. 155, 2004.
[22] A. Krieger, R. C. Susil, C. Menard, J. A. Coleman, G. Fichtinger, E. Atalar, and L. L. Whitcomb, "Design of a novel MRI compatible manipulator for image guided prostate interventions," in *IEEE Trans. on Biomedical Engineering*, vol. 52, pp. 306–313, Feb. 2005.
[23] G. Ganesh, R. Gassert, E. Burdet, and H. Bleule, "Dynamics and control of an MRI compatible master-slave system with hydrostatic transmission," in *International Confennee on Robotics and Automation*, pp. 1288–1294, Apr. 2004.
[24] D. Stoianovici, "Multi-imager compatible actuation principles in surgical robotics," in *International Journal of Medical Robotics and Computer Assisted Surgery*, vol. 1, pp. 86–100, 2005.
[25] M. J. So, S. Haker, K. H. Zou, A. S. Barnes, R. Cormack, J. P. Richie, A. V. D'Amico, and C. M. Tempany, "Clinical Evaluation of MR-guided Prostate Biopsy," in *ISMRM 13th Scientific Meeting and Exhibition*, 2005.
[26] A. Padhani, C. Gapinski, D. Macvicar, C. Parker, J. Suckling, P. Revell, M. Leach, D. Dearnaley, and J. Husband, "Dynamic contrast enhanced mri of prostate cancer: correlation with morphology and tumour stage, histological grade and psa.," in *Clin Radiol.*, vol. 55, pp. 99–109, 2000.
[27] M. R. Engelbrecht, H. J. Huisman, R. J. Laheij, G. J. Jager, G. J. van Leenders, C. A. H.-V. D. Kaa, J. J. de la Rosette, J. G. Blickman, and J. O. Barentsz, "Discrimination of prostate cancer from normal peripheral zone and central gland tissue by using dynamic contrast-enhanced MR imaging," in *Radiology*, vol. 229(1), pp. 248–254, Oct. 2003.
[28] A. Kapoor, N. Simaan, and P. Kazanzides, "A system for speed and torque control of DC motors with application to small snake robots," in *Mechatronics and Robotics*, 2004.
[29] R. J. Webster III, J. Memisevic, and A. M. Okamura, "Design Considerations for Robotic Needle Steering," in *IEEE International Conference on Robotics and Automation*, pp. 3599–3605, 2005.